Journal of Materials Chemistry C

ROYAL SOCIETY OF CHEMISTRY

PAPER

View Article Online
View Journal

Cite this: DOI: 10.1039/d0tc01173h

A crystallographic approach to the short-range ordering problem in $V_{1-x}Mo_xO_2$ ($0.50 \leq x \leq 0.60$)†

Matthew A. Davenport and Jared M. Allred *

Received 6th March 2020,
Accepted 2nd July 2020

DOI: 10.1039/d0tc01173h

rsc.li/materials-c

The $V_{1-x}Mo_xO_2$ phase diagram has high structural and electronic complexity that is driven by strong, short-range correlations that compete with the long-range rutile crystal structure. The substitution regime near 50% Mo occupancy is no exception, but there has so far been no significant progress in determining the actual structure. Reported here is a combined study using single crystal X-ray diffraction, powder X-ray diffraction, and representational analysis to examine both the local and crystallographically averaged atomic structures simultaneously near $x = 0.50$. Between about $x = 0.50$ and 0.60, the average structure of $V_{1-x}Mo_xO_2$ is the parent rutile phase, but the local symmetry is broken by atomic displacements that are best described using the orthorhombic subgroup *Fmmm*. This model is locally similar to the two-dimensionally ordered 2D-M2 phase recently reported in the compositional range $0.19 \leq x \leq 0.30$, except the correlation length is much shorter in the 2D plane, and longer in the frustrated one, making it more isotropic. This work also extends the 2D-M2 phase regime up to $x = 0.43$, and suggests that the local-*Fmmm* phase observed here can be seen as the end result of the continued suppression of the 2D-M2 phase through enhanced geometric frustration between the intrinsic order parameters. This suggests that other doped-rutile phases with elusive structures may also be dominated by similar short-range correlations that are hidden in the diffuse scattering.

Introduction

Electronic phase transitions are central to a vast array of device applications, such as sensors and switches, and they often contain a structural phase transition (SPT). In some cases, the details of the SPT are obscured, such as by convolution of multiple order parameters or from non-trivial deviations of the local structure from the crystallographically averaged one. The rutile crystal structure contains examples of this problem, mostly centring around the metal-to-insulator transition (MIT) in VO_2.[1]

The tetragonal rutile crystal structure contains infinite chains of edge-sharing metal-oxide octahedra. When the metal atoms have an open-shell, they can form metal–metal bonds along the chains. The resulting dimers necessarily break symmetry, though a few different kinds of ground states have been observed.[2] The two most common examples are both monoclinic and are colloquially known as the M1 phase and the M2 phase. In VO_2, the MIT coincides with a SPT from the high-temperature R phase with the tetragonal ideal rutile structure (R) and a low-temperature M1 phase.[3]

Taken alone, the structural instability may seem rather straightforward, but attempts to suppress or enhance it reveal hidden complexity. Doping of atoms such as niobium, molybdenum, and tungsten lead to a systematic suppression in the transition temperature while doping of other atoms such as chromium, aluminium, and gallium lead to an increased transition temperature.[4–9] In the studies of these various metal dopants, new structural phases have been discovered, such as the M2 phase which was discovered in chromium doped samples and has also been seen in aluminium doped samples, titanium doped samples, and in strained VO_2 thin films, to name a few.[6,10–12] However, some of these phases are not well defined, and the phase diagrams are frequently redrawn, with regions of uncertain provenance. In particular, the phase diagram for $V_{1-x}Cr_xO_2$—perhaps the most studied VO_2 dopant system—has been published multiple times including orthorhombic phases, other monoclinic phases called the M3 and M4 phases, and a triclinic phase called T. However, these phases and their phase boundaries are not consistent across published phase diagrams, nor are their structures well-accepted.[10,13–17] Additionally, it was only recently that the $(Ti,V)O_2$ phase diagram was shown to actually undergo spinodal decomposition.[18] These challenges all stem from the difficulty in

Department of Chemistry and Biochemistry, The University of Alabama, Tuscaloosa, AL 35487, USA. E-mail: jmallred@ua.edu

† Electronic supplementary information (ESI) available: (1) Crystallographic information file for $V_{0.45}Mo_{0.55}O_2$ in *Fmmm* space group. (CSD 2014402). (2) Detail total scattering and ΔPDF maps. See DOI: 10.1039/d0tc01173h

determining the correct structure for these doped VO_2 compounds, with the phase diagrams of other, lesser studied dopants remaining even less certain, such as Nb, Mo, and W.

We recently undertook a comprehensive total X-ray scattering study of the $V_{1-x}Mo_xO_2$ using single crystals.[19] This work showed that the M1 phase disappears suddenly between 17 and 19% Mo composition, giving way to a new phase that exhibits 2D ordering of displacements that extends to at least 27% Mo. The crystallographically averaged structure retains the R phase's 3D tetragonal symmetry, and the local symmetry is only revealed by a network of sharp scattering rods in the $HKL/2$ planes. Geometric frustration of the displacements between the [110] planes and a secondary, ferroelectric interaction along the $\langle 100 \rangle$ directions both reproduce observation and match a recent Ashkin–Teller model that is generic to the rutile structure.[20]

The correlation length, ξ, of the 2D-M2 ordering is highest (>50 Å) at $x = 0.19$ and drops substantially by $x \sim 0.40$. It seems likely that disorder, short-range correlations, and short-range ordering all play a dominant role in the structure and properties of the $V_{1-x}Mo_xO_2$ phase diagram. Indeed, previous transmission electron microscopy (TEM) measurements found evidence of supercell reflections in electron diffraction patterns around $x = 0.50$.[5] These reflections are consistent with either the M1 or M2 superstructures, but with a domain size on the order of 10 nm, and the peaks were not present in the synchrotron X-ray diffraction (PXRD) patterns, though the structural model was shown to be improved by the addition of off-site disorder on the metal site. Earlier work by Marinder in 1975, by contrast, presented evidence of two variants of the M1 phase called M1', and M1'' existing from $0.70 \leq x \leq 0.85$ and then the existence of the M2 phase below $x = 0.70$.[5,21] The researchers found that between $0.50 < x < 0.70$, the ordering is difficult to reproduce and characterize, with extensive annealing required to produce indexable powder patterns.

This study aims to clear up these inconsistencies with detailed observations about the local and long-range structure for this $0.45 \leq x \leq 0.60$ dopant regime of $V_{1-x}Mo_xO_2$, using a combination of laboratory single-crystal X-ray diffraction (SXRD), synchrotron SXRD total-scattering/3D-ΔPDF, and synchrotron PXRD. Single crystals are needed for this structural investigation because short-range structural correlations lead to very broad line-shapes and diffuse scattering features which may not be directly observable in powder diffraction. While some information can be recovered using the pair distribution function (PDF) on total scattering data, a lot of information is lost, as is shown in more detail below.

Experimental

Crystal structures were characterized using two in-house single-crystal diffractometers. The first was a Siemens diffractometer equipped with a Bruker APEX-II CCD and a monochromated Mo-Kα producing sealed source that was decommissioned during the study. The second was a Rigaku XtaLAB Synergy R, DW system, equipped with HyPix detecter. Structural models of the single crystal diffraction data were created and refined using SHELX and WINGX.[22,23] Irreducible representation analysis was aided by Isotropy by Stokes and Hatch[24] and the ISODISTORT software.[25,26]

The total scattering data was collected at the Advanced Photon Source (APS) at Argonne National Lab (ANL) on sector 6-ID-D. The experiment used an incident beam energy of 87 keV. The detector was a Dectris Pilatus CdTe 2M detector, held at a distance of 650 mm, with a threshold detection limit set to 43 keV. Samples were mounted on Kapton capillaries using either GE varnish or Duco cement. Goniometer geometry allowed free rotation of φ, limited ω, and fixed χ at 90°. Every temperature scan had three 360° φ scans, at $\omega = 0, -15, +15$. The second and third sub-scans also included a shift of the detector of 5 mm × 5 mm and 10 × 10 mm. The detector and ω shifts were to correct for gaps in the detector and blooming artefacts. The data were processed using nexpy,[27] and transformed using the crystal coordinate transformation work-flow (CCTW).[28] Sample temperature was controlled using an Oxford Cryosystems nHelix. The 3D-ΔPDF maps were created using the punch-and-fill method.[29] In this case, only the parent rutile Bragg peaks were punched, even for the $x = 0.17$ crystal, which shows long-range monoclinic symmetry.

Room temperature synchrotron PXRD data was collected at the APS using 11-BM on crystals with composition $x = 0.27$, 0.34, 0.50, 0.56, 0.59. The PXRD scans were analysed using GSAS and EXPGUI to fit a model to the data.[30,31]

The single crystals used in this study are from the same crystal growths described in detail, with complete compositional analysis in Davenport *et al.*[32] The synthesis is also summarized here for the relevant compositions. First, polycrystalline $V_{1-x}Mo_xO_2$ samples were synthesized using high purity starting materials of V_2O_3 (Alfa Aesar, 99.7%), MoO_3 (Alfa Aesar, 99.95%), and MoO_2 obtained through the reduction of MoO_3 (Alfa Aesar, 99.95%). Stoichiometric ratios of the above starting materials along with nominally 3 atm of $MoCl_3$ were sealed in an evacuated quartz tube and heated in a multi-zone furnace. The zone of the furnace containing the source powder was set to 950 °C with the tube extending into a second zone set to 850 °C. The temperatures in both zones were then held for 6 days to allow for the reaction to complete. Polycrystalline samples of $V_{1-x}Mo_xO_2$ are recovered from the hot zone, pulverized into a powder, and placed into a second sealed quartz tube with nominally 3 atm of $TeCl_4$. This tube was treated to the same heating conditions as before; yielding larger crystals of $V_{1-x}Mo_xO_2$ in the cold zone of the tube with molybdenum concentrations comparable to the initial input value.

Results and discussion

Three diffraction methods were required to characterize the structure adequately. (1) Mo-source single crystal diffraction provided initial screening of the crystals, which is how the broad peaks indicative of short-range ordering were first identified.

Subsequently, the same method was used to build the crystallographic models that are the primary result of this study. (2) Synchrotron total X-ray scattering measurements (6-ID-D) on single crystals were used to more fully map the reciprocal space (3) standard synchrotron powder X-ray diffraction (11-BM) was used to analyse the line-shape of the Bragg reflections assigned to the standard rutile structure, which gives information about the unit cell that was obscured in the single crystals.

Total scattering measurements

While hints of locally broken rutile symmetry have been reported before in the $0.45 \leq x \leq 0.60$ regime of $V_{1-x}Mo_xO_2$,[5,21] the first direct observation of the requisite diffuse scattering is shown in Fig. 1a and b. Cuts of the (hk1/2) planes (Fig. 1a) show planes of diffraction indicating the existence of a supercell structure in this dopant region. However, the peaks are extremely broad, with cross-shaped shoulders that extend far into reciprocal space, confirming that the ordering is not long-range. This peak shape explains why the previous powder and single crystal diffraction data did not agree.

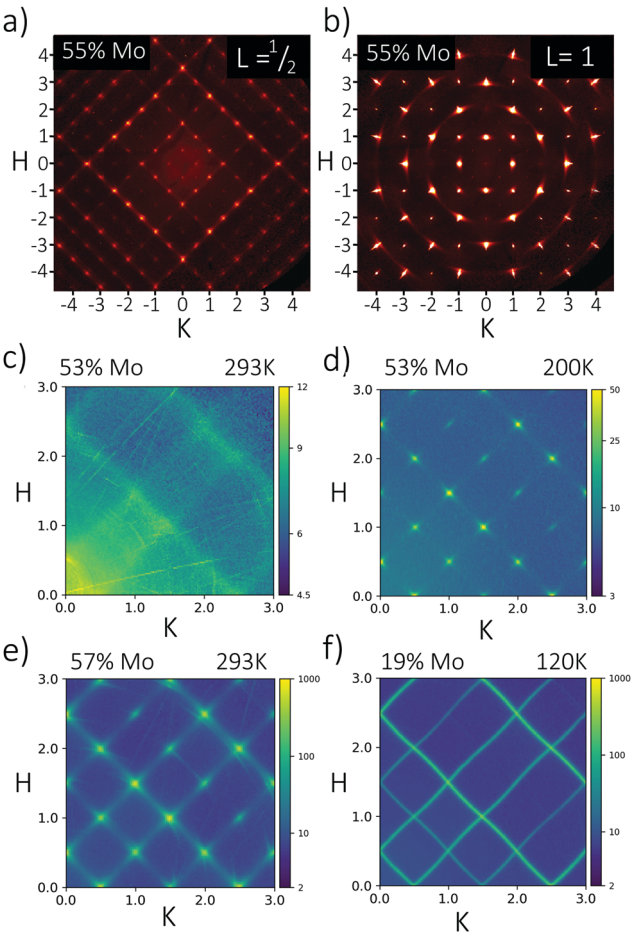

Fig. 1 Cuts of the (a) $HK\frac{1}{2}$ and the (b) $HK1$ reciprocal lattice planes in $V_{1-x}Mo_xO_2$ using the rutile lattice vectors. The presence of diffraction peaks in the (a) $HK\frac{1}{2}$ plane indicate broken $P4_2/mnm$ symmetry, but the peaks are considerably broader than usual Bragg peaks. (c–f) Total scattering data from beamline 6-ID-D at the APS. The scattering slices are all taken at L = 3/2. The 19% Mo data is shown to illustrate the 2D-M2 phase's scattering (adapted from ref. 19). All plots are in log scale.

Using the high-intensity and high-resolution of 6-ID-D, the complex Q-dependence of the supercell reflections is apparent (Fig. 1c–e). The 53.3(13)% Mo-containing material undergoes a phase transition between 200 K and 293 K. At high temperature it shows very weak diffuse scattering, while at low temperature the cross-shaped reflections are clearly visible. Below 200 K this pattern remains constant. At even higher composition, 57(1)% Mo, the ordered phase is present even at room temperature. The cross features spread further out along the same t axis and into each other, though the majority of the intensity remains at the rational HKL point. The resulting pattern of scattering rods is similar to the 2D-M2 phase observed at x = 0.19 (Fig. 1f),[19] as is the diffuse scattering pattern in high temperature x = 0.533. These scattering rods are not nearly as sharp or intense as in the actual 2D-M2. Interestingly the low temperature phase in this 50–60% Mo region does not appear to have the periodic curvature that was attributed to ferroelectric correlations along the ⟨100⟩ rutile directions, even though the high temperature scattering does. This suggests that weak 2D-M2 ordering may still be present at higher T in this compositional range.

The diffuse peaks have Lorentzian line shapes, which were used to estimate the correlation length, ξ, of the atomic displacement correlations. For x = 0.53, the peaks are relatively isotropic and the ξ = 25 and 17 Å along the narrowest and widest cross-sections perpendicular to L, respectively. By x = 0.57, ξ = 11 and 5 Å for the same axes. Compared to the 2D-M2, which has a $\xi > 50$ Å all along the 2D planes, and $\xi < 1$ nm along the other. Thus, the anisotropy is much lower here, indicating that in this higher composition region the correlations are becoming more three-dimensional, but also weaker. This might be due to overall weakened metal–metal interactions, though this occurs even as the ordering temperature is increasing. Moreover, pure MoO_2 has much stronger interactions than VO_2, so this interpretation seems unlikely. More likely is that enhanced geometric frustration, possibly due to strengthened interactions along the ⟨100⟩ directions, suppresses long-range order overall, even as the ordering becomes more isotropic.

The observed diffuse peaks correspond to a local structure deviation from the average rutile structure, rather than a new long range ordered phase. The close similarity to the scattering in the 2D-M2 phase suggests that the same local correlations are at play, even if the net result differs.

In order to understand the local structure, it is helpful to compare the displacement network to known structures. Fig. 2e shows that most of the non-lattice unit intensity in the 3D-ΔPDF maps corresponds to body-centring vectors, which are unique to inter-cationic vectors. This indicates that most of the short-range scattering arises from metal atom displacements, which is unsurprising. However, there are several known distorted rutile phases with metal atom displacements, including the M1, M2 and the less well defined M1′ and M1″ from Marinder.[21] There have also been references to even

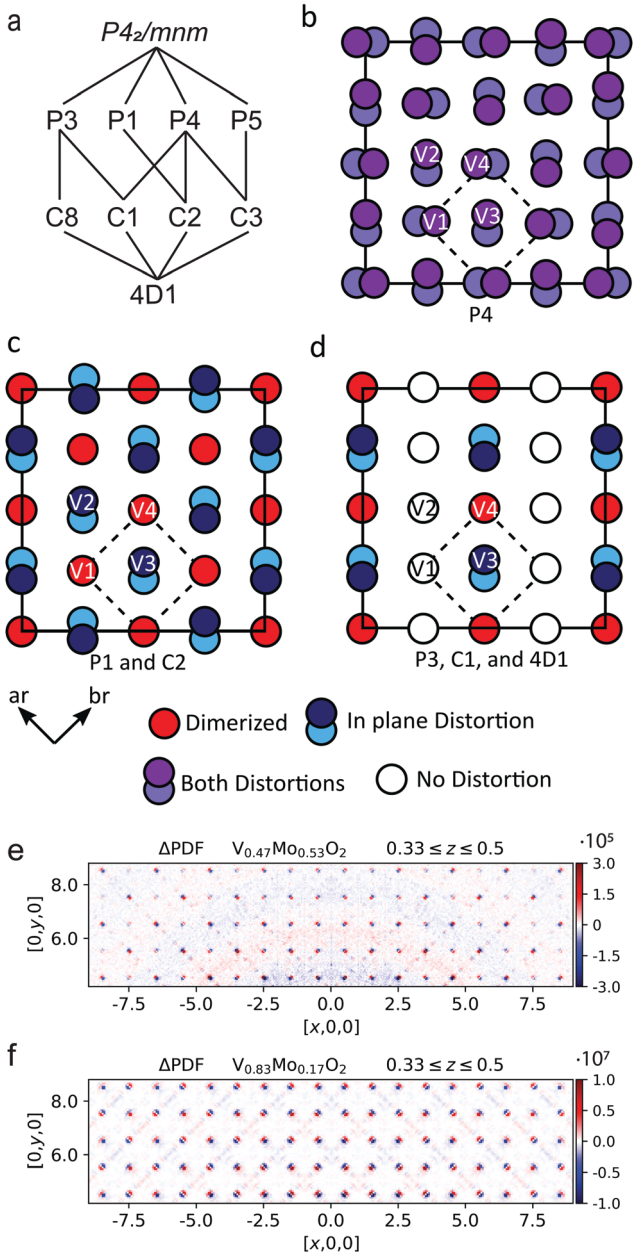

Fig. 2 (a) Group–subgroup relations under consideration. (b–d) Schematics highlighting the results of the selected structure solutions. (b) P4 is the M1 phase, (c) P1 and C2 have nearly identical models, suggesting M1 is incorrect. (d) P3 and C1 are nearly identical, and 4D1 agrees qualitatively with them as well. In 4D1, one of the "no distortion" sites has a small B2u distortion. (e) Slice at z = 0.375 from the x = 0.53 (100 K) ΔPDF map. (f) Slice at z = 0.333 from the x = 0.17 (115 K) ΔPDF map.

more monoclinic, triclinic, and orthorhombic phases that all bear resemblance to the network shown here.[13,14,16,33,34] Due to their close similarities, it is not obvious what sort of model best matches the pattern observed in the 3D-ΔPDF, and refinement methods are not yet fully validated. Moreover, the level of detail in the extracted map is not sufficient to extract local bond-lengths. Instead, other tools must be used and the PDF map will be used as a guide to help in the ensuing analysis.

It is particularly worthwhile to revisit the crystallographic approach for $V_{1-x}Mo_xO_2$ ($0.5 \leq x \leq 0.6$) in context of this new observation of the rather short-range correlations, especially given the number of proposed models over the past 5 decades. In this case, the relatively large intensity and localization around integer points mimic Bragg reflections enough to allow them to be treated as (or mistaken for) supercell peaks. This is a rare opportunity, but care must be taken due to the fundamental difference between long-range and short-range ordering. For example, structural models that appear quite different can be ambiguous in this case, due to the metrically tetragonal lattice imposed by the rutile long-range symmetry. This is because the bulk crystal necessarily contains many out-of-phase domains akin to intrinsic micro-twinning. Unlike true crystal twins, the different domains contribute to the same scattering events. Additionally, the number of possible diffracting domain orientations depends on how the chosen lattice symmetry maps onto rutile's tetragonal symmetry. Another complication is that regardless of the local symmetry, the long-range symmetry appears metrically tetragonal. This also adds an additional problem when applying the absorption correction.

Approach to the structural solutions

In order to understand the types of distortion networks that are consistent with the observed scattering intensities, isotropic group–subgroup relations were used. First, the standard laboratory SXRD (Phillips and/or Rigaku) was used to index the diffuse peaks and integrate them using a unit cell and space group deemed appropriate based on the diffuse reflections found at the R point in k-space (1/2, 0, 1/2) and/or (0, 1/2, 1/2). For the parent space group, $P4_2/mnm$, this leads to its irreducible representation (irrep) choice R_1^- as a starting point. According to ISODISTORT,[25,26] the atomic displacements in this irrep are caused by the activation of the B_{1u}, B_{2u}, and B_{3u} displacement modes for the metal atom sites and the A_1, B_1, and B_2 displacement modes for the oxygen atom sites. The metal atom displacements are thought to drive the distortion and are the strongest contributor to the scattering, and so the B_{1u}, B_{2u}, and B_{3u} are the main topic of the analysis. B_{1u} is the z-axis (dimerising) displacement, B_{2u} is the in-plane displacement along toward an oxygen, and B_{3u} is an orthogonal in-plane displacement toward an octahedral edge. B_{2u} is coupled to the B_{1u} displacement through a shared oxygen atom, while B_{3u} is not, nor is it observed in real structures.

The order parameter direction (OPD) in this irrep is a four-dimensional vector that determines the periodicity of the distortions. Each component affects each equivalent parent site, which means that the maximum number of inequivalent metal sites in the subgroup is four. Since there are three metal displacement modes, giving a maximum of there are 12 degrees of freedom which allow three Cartesian axes of the four possible metal sites, albeit with a very different basis. In this form, every metal site is displaced equally by each OPD component, which means that special displacement conditions yield different space group types. Beside the general OPD, there are eight total special OPD points in this irrep, giving a total of nine possible subgroup types in this irrep, which are listed in Table 1.

Table 1 Refinement results for the *R* (rutile) phase and all nine possible subgroups in the R_1^- irrep

Space group type (subgroup symbols)	$P4_2/mnm$ Parent	$C2/m$ (P1)	$Fmmm$ (P3)	$P2_1/c$ (P4)	$I4_1/a$ (P5)	$C2/m$ (C1)	$P\bar{1}$ (C2)	$C2/c$ (C3)	$C2/m$ (C8)	$P\bar{1}$ (4D1)
Transformation matrix	$\begin{bmatrix}1&0&0\\0&1&0\\0&0&1\end{bmatrix}$	$\begin{bmatrix}2&0&0\\0&0&2\\0&\bar{1}&0\end{bmatrix}$	$\begin{bmatrix}2&2&0\\\bar{2}&2&0\\0&0&2\end{bmatrix}$	$\begin{bmatrix}1&0&\bar{1}\\0&\bar{1}&0\\\bar{1}&0&\bar{1}\end{bmatrix}$	$\begin{bmatrix}2&0&0\\0&2&0\\0&0&2\end{bmatrix}$	$\begin{bmatrix}\bar{2}&2&0\\0&0&2\\2&0&0\end{bmatrix}$	$\begin{bmatrix}0&1&0\\1&0&1\\1&0&\bar{1}\end{bmatrix}$	$\begin{bmatrix}\bar{2}&2&0\\0&0&2\\2&0&0\end{bmatrix}$	$\begin{bmatrix}0&0&\bar{2}\\\bar{2}&\bar{2}&0\\\bar{1}&1&1\end{bmatrix}$	$\begin{bmatrix}0&0&2\\\bar{1}&1&1\\\bar{1}&\bar{1}&1\end{bmatrix}$
Origin shift	—	[0 0 1/2]	[0 0 1/2]	[1/2 0 0]	[0 1 1/2]	[0 0 1/2]	[0 0 1/2]	[1/2 1/2 0]	[0 0 1/2]	[0 0 1/2]
Displacement directions	(0,0,0,0)	(0,0,a,−a)	(a,−a,−a,a)	(0,0,a,0)	(a,a,a,−a)	(a,−a,b,−b)	(0,0,a,b)	(a,a,b,−b)	(a,b,b,a)	(a,b,c,d)
Volume per lattice point (Å^3)	62.680	125.74	252.47	126.50	252.46	254.8	125.92	252.8	252.45	252.45
R_{int}	0.0493	0.0791	0.0926	0.0531	0.0967	0.0879	0.0357	0.0927	0.1062	0.0568
R_σ	0.0087	0.0202	0.0175	0.0149	0.0181	0.0235	0.0138	0.0237	0.0269	0.0216
R_1 (all reflections)	0.0361	0.083	0.0668	0.0614	0.0921	0.0881	0.06	0.1073	0.1082	0.0941
R_1 [$F_0 > 4\sigma(F_0)$]	0.0361	0.0821	0.0631	0.061	0.0908	0.0841	0.0588	0.1028	0.1019	0.0884
wR_{0_2}	0.1028	0.1891	0.2038	0.1947	0.2848	0.2264	0.2061	0.2798	0.239	0.3191
GooF	1.187	1.202	1.302	1.142	1.3	1.254	1.123	1.279	1.18	1.299
# of refined parameters	11	40	45	31	31	71	59	59	69	115

In terms of nomenclature, each isotropic subgroup has a unique designation code given by Harold and Stokes that helps organize them into subsets. While these designations have no special meaning, it is helpful to use them to explain the connection between the nine space group choices. The four *Pn* (n = 1, 3, 4, 5) are all mutually independent, while the four C*n* (n = 1, 2, 3, 8) each have two degrees of freedom per mode. Thus, the C subset are all subgroups of at least one P type. The 4D1 contains all four degrees of freedom in each mode, making it the general point in the OPD space and the subgroup common to all the other 8 choices. All 9 choices represent extremely similar local displacements of atoms, with the differences only being represented by how many displacements are forced to be equivalent between the four possible metal sites.

To summarize, the initial structure solutions for the supercell were limited to the nine OPD options shown in Table 1, with the goal of determining which OPDs could be consistent with the observed intensities while also remaining consistent with the total X-ray scattering data (6-ID-D). As mentioned above, the apparent crystal system cannot be used to determine the space group type in this case, due to the difference between local and long-range metric symmetry. We also point out that, even if one OPD predominates, there is likely some mixing of OPDs in the boundaries between the very small domains.

Structure solution results

Structural solutions of all the options were attempted on the same data set taken from a 55% Mo sample. The reported data sets are all from the same crystal that was chosen to minimize non-merohedral twinning. Many crystals from both the same batch and from neighbouring compositions were also characterized. Most were not of suitable quality for this level of analysis, but none of the observations contradict the results detailed below.

For the chosen crystal reported here, the best twin law for improving the fit statistics was a 180° rotation about the *a* axis in the parent rutile cell, regardless of model. This twinning seems to be intrinsic to the crystal, and it is unlikely to be related to the different orientations expected from the nanoscale local ordering that come from different permutations of the same OPD. The simplest demonstration of how this can confound comparison is by noting that peaks at both (H/2,0,L/2) and (0,K/2,L/2) are observed. Some models, such as P3 and P5, index all these peaks with a single orientation, while others, such as P1 and P4, only index one set per orientation. Under normal conditions, this is routinely handled using two domains during integration or even with the appropriate twin law in SHELX. Doing so tends to improve the statistics of the P1, P4, and C2, since the software can more reliably deconvolute the domains. In the end we opted to use the same twin law mentioned above for all refinements, even though this means that some models (P1, P4, C2) are based on a fit to fewer weaker peaks. This ambiguity is dealt with later in the discussion.

The fit statistics from each model are shown in Table 1. The rutile model is used as the crystallographically averaged one; it ignores the diffuse peaks at the *R* points, and so acceptable statistics are achieved despite the effect that disorder plays. For the subgroup models, the R_{int} and R_σ generally correlate with the metric symmetry of the model. This is to be expected but does not necessarily reflect a real improvement in the model. Starting with the highest symmetry (*Pn*) models, $I4_1/a$ (P5) can be dismissed as significantly worse based on the R_1 and wR_2 values. Of $C2/m$ (P1), *Fmmm* (P3), $P2_1/c$ (P4), all are quite similar, with P3 and P4 being slightly better. However, the monoclinic P1 and P4 (the M2 and M1 phases, respectively) both benefit from a lower R_{int} value, thanks to the model using a lower point group and fewer total peaks used in data reduction and absorption correction. On the other hand, *Fmmm* (P3) is able to produce a final *R* value comparable to the others without assuming lower symmetry in the absorption correction.‡ In this context, this

‡ The *R* values would normally be considered rather high for a normal structural solution, but one must adjust their standards according to the real system under study. For example, the *R* values are not dissimilar to extended inorganic crystals with stacking faults and correlated occupancy order.[37]

information alone is not enough to rule out P1, P3, or P4 as a valid OPD for describing the local metal distortions, though P5 appears unlikely.

Schematics of the metal atom displacements are shown for the viable P1, P3, and P4 models in Fig. 2b–d. The three models all show different atomic displacement patterns. In P1, only half of metal atoms allow B_{1u} dimerization, the other half B_{2u}, giving 2 unique metal sites. In P3, all four metal sites are unique, with B_{1u}, B_{2u}, and B_{3u} all being mutually exclusive and a fourth metal site remaining fixed. P4 has only unique metal site, where all atoms have equivalent distortion modes. Another way that the models differ is in the determined bond lengths. Note that the M–M bond length in VO_2 is 2.65 Å and in MoO_2 it is 2.51 Å. Only the *Fmmm* (P3) model produces a bond length in this range (2.60 Å). The other two candidates, P1 and P4, have determined M–M bond lengths of 2.71 and 2.75 Å, respectively.

Moving on to the C*n* set can help clarify some of these issues, since they can be compared against their supergroups. $P\bar{1}$ (C2) contains a degree of freedom for each of the known M1 and M2 cells (P4 and P1), and shows overall the best statistics on the table at first glance. Comparing these three structures, the C2 model is found to agree more closely with the M2 (P1) structure than the M1 (P4) structure (Fig. 2c). However, there are slight differences that do hybridize the M1 and M2 structures slightly. This seems to suggest that extra degrees of freedom seem to prefer an OPD that allows for inequivalent metal sites, which would rule out M1 (P4) as the best interpretation.

There is a crucial caveat to this interpretation. To wit, changing the twin law chosen between the *a* and *b* rutile axes has a tiny effect on the *R* values. The model remains M2-like, though it does cause a significant shift toward the M1-like model. This illustrates the difficulty in blindly applying crystallographic tools to disordered but correlated systems. The reason this occurs can be seen in Table 1. C2, P1, and P4 have the OPDs $(0,0,a,b)$, $(0,0,a,-a)$ and $(0,0,a,0)$, respectively. These are only example sets, as many permutations are equivalent, such as $(a,0,0,0)$ for P4 or $(a,-a,0,0)$ for P1. C2 becomes P1 if $|b| = |a|$ and it becomes P4 if either $a = 0$ or $b = 0$. This is an issue because, as mentioned above, the scattering intensity in $V_{0.45}Mo_{0.55}O_2$ is not a superposition of all the different crystal domains, which is what a twin law assumes. Instead, it is a convolution of them, since in this case most scattering events arise from pairs in different coherent domains. For example, the superposition of the two adjacent M1 (P4) OPDs $(0,0,a,0)$ and $(0,0,0,-a)$ would produce scattering similar to $(0,0,a,-a)$, which is M2 (P1). Alternatively, the inverse is true, and a P1 domain could be treated as the superposition of two P4 domains of the appropriate orientations using a spurious twin law. This argument can be extended further, as any P*n* OPD could be constructed from the superposition of enough domains of some others. For example, *Fmmm* (P3) has the OPD $(a,-a,-a,a)$, which could be the superposition of two M2 (P1) or four M1 (P4) domains. In this context, the refined C2 structure might be seen as the superposition of multiple domains of either the P1 or P4, with the absolute population determining the structure. Normally the crystal system or Laue class could be used to narrow this down, but this crystal is metrically tetragonal. Luckily, complementary observations are available that can be used to narrow down the options, which will be detailed below.

Setting aside the M1 (P4) for now, we turn our attention to the M2 (P1) and *Fmmm* (P3) models. A similar comparison of these models can be achieved using another structure possibility, *C*2/*m* (C1), of which both the *C*2/*m* (P1) and *Fmmm* (P3) models are substructures. This comparison shows that the C1 model barely differs from the *Fmmm* (P3) model. *Fmmm* provides the best structural solution of the structural models with only one degree of freedom out of the four irrep modes. The same is true of the C8 model, which is a subgroup of only P3, but does not differ from P3 in this structure solution. A further comparison can be done with the $P\bar{1}$ (4D1) model option of which all eight other options are substructures since the 4D1 model option allows the magnitude for each distortion direction to be different. While this structure does show slight additional distortions compared to that allowed by the *Fmmm* structure (Table 2), these differences are very small. This provides further evidence that the *Fmmm* model is the best description for this short range ordered phase.

Switching from a Cartesian coordinate system to an irrep one clarifies what kind of degrees of freedom are necessary to reproduce the scattering intensity.[35] Table 3 compares the magnitude of each mode for the M1 (P4), M2 (P1), *Fmmm* (P3), C1, C2, and 4D1 structural models (Table 3). This comparison sees a trend in which the magnitude of the B_{1u} and the B_{2u} modes increase going from M1 (P4) to M2 (P1) to *Fmmm* (P3). The larger magnitudes of these modes result in shorter dimers and more drastic antiferroelectric distortions in the *Fmmm* (P3) solution compared to both the M1 (P4) and M2 (P1) models (Table 2). The maximized distortions in the *Fmmm* (P3) model are relevant because each distortion can only occur at 1/4 of the metal atom sites while 1/2 of the metal atom sites stay

Table 2 The difference between the long and short distances between the 4 metal atom sites as well as the angle of metal atom chains

	R	M1	M2	C2	P3 (*Fmmm*)	C1	4D1
ΔV1	0	0.189(1)	0.263(1)	0.2511(11)	0	0.008(2)	0.023(4)
ΔV2	0	0.189(1)	0	0.0372(11)	0	0	0.105(6)
ΔV3	0	0.189(1)	0	0.0372(11)	0	0	0.183(6)
ΔV4	0	0.189(1)	0.263(1)	0.2511(11)	0.477(3)	0.457(2)	0.432(4)
∠V1	180	177.92(5)	180	179.52(5)	180	180	177.94(9)
∠V2	180	177.92(5)	176.87(7)	177.14(5)	178.75(8)	178.60(6)	178.53(4)
∠V3	180	177.92(5)	176.87(7)	177.14(5)	174.24(7)	173.75(9)	174.37(6)
∠V4	180	177.92(5)	180	179.52(5)	180	180	178.66(9)

Table 3 Values for the metal atom displacement modes for the P4, P1, C2, P3, C1, and 4D1 models. In the setting used here, B_{1u} is the dimerizing metal displacement, B_{2u} is the in-plane distortion coupled to the dimerization, and B_{3u} is the in-plane distortion orthogonal to B_{2u}

Displacement Mode	$P2_1/c$ (P4)	$C2/m$ (P1)	$P\bar{1}$ (C2)	$Fmmm$ (P3)	$C2/m$ (C1)	$P\bar{1}$ (4D1)
B_{1u} (a)	−0.09922	−0.09685	−0.07472	0.16657	−0.11704	−0.06919
B_{1u} (b)	—	—	0.05508	—	0.1126	0.09632
B_{1u} (c)	—	—	—	—	—	−0.01377
B_{1u} (d)	—	—	—	—	—	0.12945
B_{2u} (a)	0.05455	0.05622	0.04237	−0.11244	0.0809	0.04711
B_{2u} (b)	—	—	−0.03043	—	−0.07864	−0.06138
B_{2u} (c)	—	—	—	—	—	0.01445
B_{2u} (d)	—	—	—	—	—	−0.07846
B_{3u} (a)	−0.0138	−0.00929	−0.00853	0.0199	−0.01905	−0.01145
B_{3u} (b)	—	—	0.00826	—	0.01852	0.01577
B_{3u} (c)	—	—	—	—	—	−0.00328
B_{3u} (d)	—	—	—	—	—	0.02149

undistorted. On the other hand, in the M2 phase, every metal atom position undergoes a distortion with 1/2 forming dimer pairs and 1/2 forming antiferroelectric distortions, and in the M1 phase every metal atom undergoes both dimerization and antiferroelectric distortions. With this in mind, it seems that the weaker distortions contained in the M1 (P3) and M2 (P1) models are likely a result of an artificial averaging between a strongly distorted chain and a weakly or undistorted chain of metal atoms, as discussed above. It does not make sense that the average bond-length between Mo–Mo, V–V, and Mo–V would be so much larger than it is in either VO_2 or MoO_2. Only the *Fmmm* (P3) model falls in the correct range (2.50 Å ≤ 2.60 Å ≤ 2.65 Å). Overall, the bond mode analysis supports P3 as the OPD that most closely represents the local atomic displacements.

Further evidence of this comes from comparing the *Fmmm* structure solution to lower symmetry ones. The intermediate C1 phase is exactly equal to the *Fmmm* when the mode magnitudes are $a = -b$. This is very close to what was found (Table 3) for all three modes. In the lowest symmetry, 4D1 structure solution, every atom is allowed to undergo distortions by the 4 individual degrees of freedom. The structural refinement results in a structure nearly identical to the *Fmmm* (P3) phase with 1/4 of the metal atom chains undergoing strong dimerization, 1/4 of the chains undergoing strong antiferroelectric distortions, and only weak dimerization and antiferroelectric distortions in the chains where those distortions are not allowed by the *Fmmm* structure. The crystal structure results for the *Fmmm* (P3) structure are given in detail in Tables 4 and 5. Notably, none of the attempted models show any evidence of significant occupancy ordering.

Finally, we return to the total scattering and 3D-ΔPDF for additional guidance. The maps for the $x = 0.53$ sample in the low temperature phase is difficult to distinguish from the generated map from the long-range M1-type phase found in the $x = 0.17$ composition (cuts from each are shown in Fig. 2e and f, respectively). This is not unexpected since similar displacements exist in all structures, and the data shows a superposition of all vectors. There are some subtle differences between the two maps. Firstly, there is a checkerboard modulation of intensity in the $x = 0.55$ map. One half of the intermetallic origin-to-body (or v.v.) vectors are significantly weaker than the rest, with the in-plane displacements along the nearest diagonal being stronger than those rotated 90°. This observation rules out a pure M1 (P4) type structure, as the displacements must be equal for all sites, which is observed in the $x = 0.17$ map. Another difference is that these same features are much narrower in the $x = 0.53$ map, indicative of less mixing of both orientations of in-plane displacements. More detailed views are available in Fig. S2 in the ESI.†

Instead, both observations are more reminiscent of the 2D-M2 phase[19] found between $x = 0.19$ and 0.43 (see ESI†), except here the correlations extended further along the axis perpendicular to the M2-like planes. This pattern would be explained by the superposition of two different orientations of a striped model, either M2 (P1) or *Fmmm* (P3), that is rotated by 90° about the *c* axis. Both models have in-plane displacements

Table 4 Structural refinement parameters for the structural solution of $V_{0.45}Mo_{0.55}O_2$ using the space group *Fmmm*

a (Å)	13.3365(9)
b (Å)	13.3352(10)
c (Å)	5.6785(3)
α (°)	90
β (°)	90
γ (°)	90
V (Å^3)	1009.89(12)
Z	32
Temperature (K)	293(2)
θ_{max}	42.59
Crystal description	Plate
Crystal colour	Metallic-bluish-black
Crystal size (mm)	0.16 × 0.12 × 0.05
Scan mode	ω
Absorption coefficient mu (mm^{-1})	8.577
Absorption correction	Numerical
T_{min}/T_{max}	0.302/0.651
radiation wavelength (Å)	0.71073
F_{000}	1584
# of unique reflections	1186
R_{int}	0.0926
R_σ	0.0175
R_1 (all reflections)	0.0668
R_1 [$F_0 > 4\sigma(F_0)$]	0.0631
wR_2	0.2038
$G_{00}F$	1.302
# of refined parameters	45

Table 5 Structural solution approximating the local structure if $V_{0.45}Mo_{0.55}O_2$ in the space group *Fmmm*

Site	x	y	z	Wyckoff	U_{eq}	Occupancy
V1/Mo1	0	0	0.72902(13)	8i	0.0175(2)	0.48/0.52 (2)
V2/Mo2	1/4	3/4	3/4	8f	0.0230(3)	0.48/0.52 (2)
V3/Mo3	0	0.75536(6)	0	8h	0.0208(2)	0.43/0.57 (2)
V4/Mo4	0.24884(7)	0	0	8g	0.0247(2)	0.40/0.60 (2)
O1	0	0.903(3)	0	8h	0.0183(7)	1
O2	0.2494(3)	0.1484(3)	0	16o	0.0218(6)	1
O3	0.8549(2)	0	0.7470(6)	16n	0.0157(5)	1
O4	0.1050(2)	3/4	3/4	16l	0.0160(5)	1
O5	0	0.6070(4)	0	8h	0.0226(8)	1

Site	U_{11}	U_{22}	U_{33}	U_{12}	U_{13}	U_{13}
V1/Mo1	0.0228(6)	0.0161(5)	0.0136(3)	—	—	—
V2/Mo2	0.0218(6)	0.0161(6)	0.0309(5)	—	—	—
V3/Mo3	0.0152(5)	0.0190(4)	0.0284(3)	—	—	—
V4/Mo4	0.0166(6)	0.0264(7)	0.0311(4)	—	—	—
O1	0.022(2)	0.0177(17)	0.0154(15)	—	—	—
O2	0.0210(17)	0.029(2)	0.0155(9)	0.0013(11)	—	—
O3	0.0156(12)	0.0185(14)	0.0130(8)	—	0.0001(8)	—
O4	0.0155(12)	0.0187(14)	0.0137(8)	—	—	0.0000(8)
O5	0.021(2)	0.031(3)	0.0160(16)	—	—	—

along a single axis and they are also identical within a particular (110) slice. The presence of weak stripes and strong stripes could be used as evidence in support of a P3 like OPD, which has stripes of low displacement correlations in our crystallographic model. Even so, caution against overinterpretation is warranted at this stage, due to the possibility of confounding features. It is certainly possible that a M2 (P1) model could be made compatible with the observed stripes under the right conditions, and so more work on applying the 3D-ΔPDF technique is needed.

Discussion of the proposed (P3) *Fmmm* model

Altogether, our analysis supports the interpretation of a P3-like local-structure in the title compounds. Tables 4 and 5 report the structural solution of the *Fmmm* model. The model exhibits stripes of distorted and undistorted metal sites, with no evidence of metal-site ordering nor preferential bond formation for either V or Mo. Note that while the model implies long-range ordering, the real structure is disordered beyond about a dozen unit cells, and it should be assumed that a very large range of local environments are present, especially near domain boundaries.

The model also suggests that there are alternating planes of distorted and non-distorted atoms, which matches the local structure of the 2D-M2 phase.[19] In the 2D-M2 case, there are very weak short-range correlations between planes that are an odd number of unit cells apart. This unusual observation was predicted by the geometric frustration model of Lovorn and Sarker.[20] This does not necessarily mean that every other plane is undistorted (though it could), only that there are no strong correlations between neighbouring planes, and so they average out over multiple unit cells. That would mean that actually all atoms show some distortion, with 50% dimerized, but the correlations between half of the atoms in the unit cell are too weak to observe. In this sense, the *Fmmm* model can be seen as a special condition of the M2 state, even though it is a monoclinic lattice.

It is not clear which way the local *Fmmm* model should be interpreted in this compound, though either interpretation leads to a unique structural motif. We are not aware of any system that contains alternating layers of displacement networks that are interlaced but partially decoupled one with the other, though this would be the realization of the Lovorn and Sarker hypothetical 'embedded 2D-crystal' model. The other option, with alternate layers that are distorted and undistorted, is also unusual. It had previously been proposed in the Cr-doped phase diagram by Pierce and Goodenough, though they used the space group *F*222, which diverges from the P3 OPD only minimally.[33] Goodenough later retracted this model in favour of the M2 phase, when the lattice was revealed to be monoclinic.[16] Nevertheless, we have shown that even with extreme care there is room for ambiguity, as the 55% Mo specimen would have been intractable without an understanding of the short-range nature of the distortions. We suggest that attention to short-range correlations in the Cr phase diagram may reveal similar complications to those we uncovered here.

Powder diffraction

The single crystal model only refines atomic positions against a list of measured F^2, meaning that it does not contain any information about the unit cell that was not determined from the integration step. However, if the local structure is most similar to orthorhombic *Fmmm*, then the metric symmetry must be lowered from tetragonal on the length same scale, in this case by making $\gamma \neq 90^\circ$ in the parent cell. Unfortunately, the long-range symmetry is tetragonal, so that is the apparent symmetry of the model, regardless of the actual local structure. The *Fmmm* model's apparent a and b lattice parameters are essentially equal. As an alternate probe, powder diffraction can be extremely sensitive to small changes in lattice parameters, and it is insensitive to crystallite orientation. Additionally, utilizing anisotropic broadening of peaks within the Rietveld

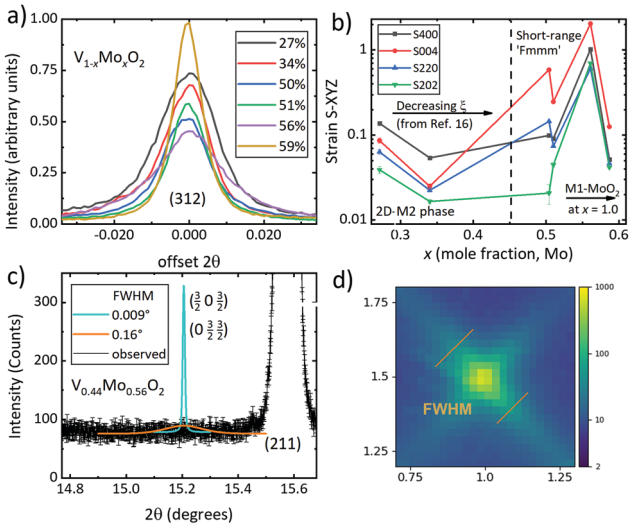

Fig. 3 PXRD data on $V_{1-x}Mo_xO_2$ from 11-BM at room temperature. (a) Comparison of peak shape between compositions. Peaks are both normalized and offset in 2θ for comparison. (b) Anisotropic peak broadening and strain analysis as a function of composition from Rietveld refinement using a rutile model (c) Comparison between expected supercell reflection (3/2 0 3/2) and observation in $V_{0.44}Mo_{0.56}O_2$ for two different line-widths. The intensity is equivalent in both, and is taken from the single crystal diffraction integrated intensities. The blue line has the same FWHM as the observed parent phase reflections in this composition (*e.g.* panel a). The orange line uses the actual FWHM determined from total scattering (6-ID-D), shown in panel (d).

method allows an accurate correlation between peak shape and local strain, or in other words, deviation from tetragonality.

Synchrotron powder diffraction data (11-BM) were collected in the composition range x = 0.20 to 0.60 and x = 1.0 at room temperature. The peak shape of the (312) reflection are shown in Fig. 3a. Above x = 0.40, the peak broadens substantially, with the FWHM maximized at x = 0.55. Note that this is around where the transition must go above room temperature. The broadening of the rutile peaks is likely directly correlated to the short-range correlations. In order to get a qualitative sense of whether strain is lowering the local symmetry, the Stephens anisotropic strain broadening terms were refined using the rutile cell as the model, shown in Fig. 3b.[36] The strain is quite high along all axes, suggesting a local structure with a different metric symmetry than the parent, which is yet another piece of evidence against the tetragonal $I4_1/a$ (P5) OPD.

Finally, there are no observed peaks in the PXRD pattern that are consistent with the supercell (Fig. 3c), as expected. Based on the total scattering data (Fig. 3d), the diffuse reflections are about 0.26° FWHM, which is unobservable (Fig. 3c, orange line). Interestingly, even without the super-cell peaks present in the fit, the intensities of the subcell reflections can still be used to fit the same models, with similar results to the SXRD, albeit much less accurately. This is because the subcell peaks do contain some information about the local displacements, and it is the coherence between displacements that is missing without the supercell peaks.

Conclusions

We have shown that $V_{1-x}Mo_xO_2$ ($0.50 \leq x \leq 0.60$) departs from the rutile symmetry below a phase transition that crosses above room temperature between 53 and 57% Mo. The long-range crystal structure is rutile, but there are strong local correlations that give rise to a phase with a distorted structure attributed to the R_1^- irrep in the $P4_2/mnm$ space group type. The metal atom displacements were found to most likely correspond to the P3, $(a,-a,-a,a)$, order parameter direction in this irrep which would lead to the orthorhombic *Fmmm* space group as a crystalline phase. The phase cannot be perfectly ordered as evidenced by the broad, cross shaped diffraction peaks observed in total scattering data. The solution of this structural phase helps to increase the understanding of the $V_{1-x}Mo_xO_2$ phase diagram as well as the VO_2 system in general since the same structural determination used for this phase can be applied to other related dopant phases that have structures which have proven difficult to understand. The model is similar to the planar structure of the newly reported 2D-M2 phase at lower Mo compositions,[19] and can be seen as the collapse of the 2D-M2 into one that has very short-range ordering that is roughly equal in all 3 dimensions instead of just one. This is a culmination of the geometric frustration that gives rise to the 2D-M2 ordering.

Isotropic group–subgroup relations were invaluable to the structure solution. Future work in more completely mapping out the group–subgroup space of the known rutile distortions would further resolve many of the existing inconsistencies. While the 3D-PDF data has been very helpful in comparing the crystallographic interpretation of the short-range model, further work in developing a model that explains the entire $V_{1-x}Mo_xO_2$ phase diagram is required.

Conflicts of interest

There are no conflicts to declare.

Acknowledgements

The work was supported by the U.S. Department of Energy, Office of Basic Energy Sciences under award DE-SC0018174. For synchrotron data from beamlines 6-ID-D and 11-BM-B, use of the Advanced Photon Source at Argonne National Laboratory was supported by the U. S. Department of Energy, Office of Science, Office of Basic Energy Sciences, under Contract No. DE-AC02-06CH11357. The authors thank NSF CHE MRI 1828078 and UA for the purchase of the single crystal X-ray diffraction instrument used in this study. We also thank Dr Matthew J. Krogstad and Dr Ray Osborn for help with the total scattering data processing and for helpful discussions when writing and revising this work. We thank Dr Stephan Rosenkranz and Dr Doug Robinson for support during the 6-ID-D experiment.

Notes and references

1 F. J. Morin, *Phys. Rev. Lett.*, 1959, **3**, 34–36.
2 Z. Hiroi, *Prog. Solid State Chem.*, 2015, **43**, 47–69.

3 W. H. Brito, M. C. O. Aguiar, K. Haule and G. Kotliar, *Phys. Rev. Lett.*, 2016, **117**, 056402.
4 G. Villeneuve, A. Bordet, A. Casalot, J. P. Pouget, H. Launois and P. Lederer, *J. Phys. Chem. Solids*, 1972, **33**, 1953–1959.
5 K. L. Holman, T. M. McQueen, A. J. Williams, T. Klimczuk, P. W. Stephens, H. W. Zandbergen, Q. Xu, F. Ronning and R. J. Cava, *Phys. Rev. B.*, 2009, **79**, 245114.
6 J. P. Pouget, H. Launois, T. M. Rice, P. Dernier, A. Gossard, G. Villeneu and P. Hagenmul, *Phys. Rev. B: Condens. Matter Mater. Phys.*, 1974, **10**, 1801.
7 P. Jin and S. Tanemura, *Jpn. J. Appl. Phys.*, 1995, **34**, 2459–2460.
8 Y. Wu, L. Fan, S. Chen, S. Chen, F. Chen, C. Zou and Z. Wu, *Mater. Lett.*, 2014, **127**, 44–47.
9 L. Kang, Y. Gao, Z. Zhang, J. Du, C. Cao, Z. Chen and H. Luo, *J. Phys. Chem. C*, 2010, **114**, 1901–1911.
10 M. Marezio, B. McWhan, J. P. Remeika and P. D. Dernier, *Phys. Rev. B: Condens. Matter Mater. Phys.*, 1972, **5**, 2541–2551.
11 M. Ghedira, H. Vincent, M. Marezio and J. C. Launay, *Solid State Chem.*, 1977, **22**, 423–438.
12 T. Kong, M. W. Masters, S. L. Bud'ko and P. C. Canfield, *APL Mater.*, 2015, **3**, 041502.
13 G. Villeneuve, M. Drillon and P. Hagenmulier, *Mater. Res. Bull.*, 1973, **8**, 1111–1122.
14 P. Hagenmuller, *NBS Spec. Publ.*, 1972, **364**, 205–218.
15 G. Villeneuve, A. Bordet, A. Casalot and P. Hagenmuller, *Mater. Res. Bull.*, 1971, **6**, 119–130.
16 J. B. Goodenough and H. Y. P. Hong, *Phys. Rev. B: Condens. Matter Mater. Phys.*, 1973, **8**, 1323–1331.
17 Z. Shao, X. Cao, H. Luo and P. Jin, *NPG Asia Mater.*, 2018, **10**, 581–605.
18 Z. Hiroi, H. Hayamizu, T. Yoshida, Y. Muraoka, Y. Okamoto, J. Yamaura and Y. Ueda, *Chem. Mater.*, 2013, **25**, 2202–2210.
19 M. A. Davenport, M. J. Krogstad, L. M. Whitt, H. Hu, T. C. Douglas, N. Ni, S. Rosenkranz, R. Osborn and J. M. Allred, arXiv:1909.12704, 2019.
20 T. Lovorn and S. K. Sarker, *Phys. Rev. Lett.*, 2017, **119**, 045501.
21 B. O. Marinder, *Mater. Res. Bull.*, 1975, **10**, 909–914.
22 G. M. Sheldrick, *Acta. Cryst.*, 2008, **64**, 112–122.
23 L. J. Farrugia, *J. Appl. Crystallogr.*, 1999, **32**, 837–838.
24 H. T. Stokes and D. M. Hatch, *Isotropy Subgroups of the 230 Crystallographic Space Groups*, World Scientific, 1989.
25 B. J. Campbell, H. T. Stokes, D. E. Tanner and A. D. M. Hatch, *J. Appl. Crystallogr.*, 2006, **39**, 607–614.
26 H. T. Stokes, D. M. Hatch and B. J. Campbell, ISODISTORT, ISOTROPY Software Suite, https://stokes.byu.edu/iso/isodistort.php.
27 NeXpy: A Python GUI to analyze NeXus data, http://nexpy.github.io/nexpy/.
28 G. Jennings, R. Osborn and J. Wozniak, Crystal Coordinate Transformation Workflow, https://www1.aps.anl.gov/science/scientific-software/cctw.
29 M. J. Krogstad, S. Rosenkranz, J. M. Wozniak, G. Jennings, J. P. C. Ruff, J. T. Vaughey and R. Osborn, *Nat. Mater.*, 2019, **18**, 1384.
30 B. H. Toby, *J. Appl. Crystallogr.*, 2001, **34**, 210–213.
31 A. C. Larson and R. B. V. Dreele, *Los Alamos Natl. Lab., [Rep.] LA (U. S.)*, 2000, **86–748**.
32 M. A. Davenport, M. P. Confer, T. C. Douglas, T. B. R. Chettri and J. M. Allred, *Cryst. Growth Des.*, 2020, **20**, 3635–3640.
33 J. W. Pierce and J. B. Goodenough, *Phys. Rev. B: Condens. Matter Mater. Phys.*, 1972, **5**, 4104–4111.
34 X. Tan, W. Liu, R. Long, X. Zhang, T. Yao, Q. Liu, Z. Sun, Y. Cao and S. Wei, *J. Phys. Chem. C*, 2016, **120**, 28163–28168.
35 S. Kerman, B. J. Campbell, K. K. Satyavarapu, H. T. Stokes, F. Perselli and J. S. O. Evans, *Acta Crystallogr., Sect. A: Found. Crystallogr.*, 2012, **68**, 222–234.
36 P. Stephens, *J. Appl. Crystallogr.*, 1999, **32**, 281–289.
37 J. M. Allred, L. M. Wang, P. Khalifah and R. J. Cava, *J. Solid State Chem.*, 2010, **184**, 44–51.

